

V-Co: A Closer Look at Visual Representation Alignment via Co-Denoising

Han Lin¹ Xichen Pan² Zun Wang¹ Yue Zhang¹ Chu Wang³ Jaemin Cho⁴ Mohit Bansal¹

¹UNC Chapel Hill ²NYU ³Meta ⁴AI2

<https://github.com/HL-hanlin/V-Co>

Abstract

Pixel-space diffusion has recently re-emerged as a strong alternative to latent diffusion, enabling high-quality generation without pretrained autoencoders. However, standard pixel-space diffusion models receive relatively weak semantic supervision and are not explicitly designed to capture high-level visual structure. Recent representation-alignment methods (e.g., REPA) suggest that pretrained visual features can substantially improve diffusion training, and visual co-denoising has emerged as a promising direction for incorporating such features into the generative process. However, existing co-denoising approaches often entangle multiple design choices, making it unclear which design choices are truly essential. Therefore, we present **V-Co**, a systematic study of visual co-denoising in a unified JiT-based framework. This controlled setting allows us to isolate the ingredients that make visual co-denoising effective. Our study reveals four key ingredients for effective visual co-denoising. First, preserving feature-specific computation while enabling flexible cross-stream interaction motivates a fully dual-stream architecture. Second, effective classifier-free guidance (CFG) requires a structurally defined unconditional prediction. Third, stronger semantic supervision is best provided by a perceptual-drifting hybrid loss. Fourth, stable co-denoising further requires proper cross-stream calibration, which we realize through RMS-based feature rescaling. Together, these findings yield a simple recipe for visual co-denoising. Experiments on ImageNet-256 show that, at comparable model sizes, V-Co outperforms the underlying pixel-space diffusion baseline and strong prior pixel-diffusion methods while using fewer training epochs, offering practical guidance for future representation-aligned generative models.

1. Introduction

Diffusion models [13, 29, 33] have achieved remarkable success in image generation. While much recent progress has been driven by latent diffusion models [34] (LDMs),

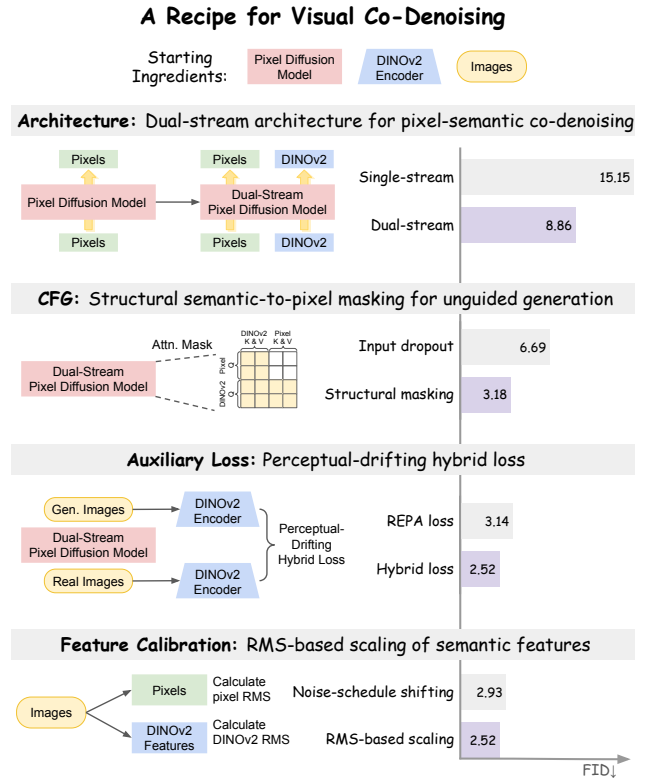


Figure 1. **An overview of V-Co and its recipe.** Starting from a pixel diffusion model, a pretrained DINOv2 encoder, and training images, we identify four key ingredients for effective visual co-denoising: a fully dual-stream architecture, semantic-to-pixel masking for classifier-free guidance, a perceptual-drifting hybrid loss for stronger semantic supervision, and RMS-based feature rescaling for cross-stream calibration. Together, they form a simple and effective recipe for visual co-denoising.

which denoise in compressed autoencoder spaces [23, 34], an increasingly compelling alternative is pixel-space diffusion with scalable Transformer-based denoisers [6, 26, 28, 31, 48]. Recent systems such as JiT [26] show that direct pixel-space denoising can be competitive while avoiding autoencoder-induced biases and bottlenecks. However,

pixel-level denoising objectives are not explicitly designed to enforce high-level semantic structure, making semantic representation learning less sample-efficient.

In parallel, a growing body of work has explored how to inject external visual knowledge from strong pretrained encoders into diffusion training. One line of research adds *representation-alignment losses* that encourage diffusion features to match pretrained visual representations [35, 36, 39, 42, 49, 51]. Another performs denoising directly in a *representation latent space*, rather than in pixel or VAE latent space [3, 18, 37, 50]. A third line of work explores *joint generation or co-denoising* architectures, in which image latents are generated together with semantic features or other modalities so that the streams can exchange information throughout the denoising trajectory [1, 2, 4, 8, 9, 14, 19, 24, 43, 45, 52]. Among these directions, visual co-denoising provides a deeper form of integration by incorporating pretrained semantic representations directly into the denoising process, rather than using them only as supervision or as an alternative latent space. However, existing co-denoising systems typically entangle multiple design choices, spanning architecture, guidance strategy, auxiliary supervision, and feature calibration, which obscures the principles that govern effective pixel-semantic interaction. This lack of understanding makes current designs largely ad hoc, and leaves open how to combine these components into a robust and scalable recipe.

In this paper, we study visual co-denoising as a mechanism for visual representation alignment. Rather than treating co-denoising as a fixed end-to-end design, we investigate the factors that makes it effective. To this end, we build a unified pixel-space testbed on top of JiT [26], where an image stream is jointly denoised with patch-level semantic features from a frozen pretrained visual encoder (e.g., DINOv2 [32]). Within this controlled framework, we investigate four key questions: **(i)** what architecture best balances feature-specific processing and cross-stream interaction; **(ii)** how to define the unconditional branch for classifier-free guidance; **(iii)** which auxiliary objectives provide the most effective complementary supervision; and **(iv)** how to calibrate semantic features relative to pixels during diffusion training. Our goal is not only to improve performance, but also to distill general principles for effective co-denoising.

Based on this study, we derive a simple yet effective **Visual Co-Denoising (V-Co)** recipe, illustrated in Fig. 1. First, from the perspective of model architecture, we show that effective visual co-denoising requires preserving feature-specific computation while enabling flexible cross-stream interaction. Among a broad range of shared-backbone and fusion-based variants, a *fully dual-stream* JiT consistently delivers the strongest performance (Sec. 3.2). Second, for classifier-free guidance (CFG), we introduce a novel *structural masking* formulation, where unconditional

prediction is defined by explicitly masking the semantic-to-pixel pathway rather than by input-level corruption alone. This simple design proves substantially more effective than standard dropout-based alternatives in co-denoising (Sec. 3.3). Third, we observe that instance-level semantic alignment and distribution-level regularization play complementary roles, and leverage this insight to propose a novel *perceptual-drifting hybrid loss* that combines both within a unified objective, yielding the best generation quality in our study (Sec. 3.4). Finally, we show that RMS-based feature rescaling admits an equivalent interpretation as a semantic-stream noise-schedule shift via signal-to-noise ratio (SNR) matching, providing a simple and principled calibration rule for cross-stream co-denoising (Sec. 3.5). Together, these findings transform visual co-denoising into a concrete recipe for visual representation alignment.

Empirically, V-Co yields strong gains on ImageNet-256 under the standard JiT [26] training protocol. Starting from a pixel-space JiT-B/16 backbone, our progressively improved recipe substantially outperforms both the original JiT baseline and prior co-denoising baselines (see Table 5), and achieves strong guided generation quality. Notably, V-Co-B/16 with only 260M parameters, matches JiT-L/16 with 459M parameters (FID 2.33 vs. 2.36). V-Co-L/16 and V-Co-H/16, trained for 500 and 300 epochs respectively, outperform JiT-G/16 with 2B parameters (FID 1.71 vs. 1.82) and other strong pixel-diffusion methods.

In summary, our contributions are three-fold:

- We present a principled study of visual representation alignment via co-denoising (**V-Co**) in pixel-space diffusion, systematically isolating the effects of architecture, CFG design, auxiliary losses, and feature calibration.
- We introduce an effective recipe for visual co-denoising with two key innovations: *structural masking* for unconditional CFG prediction and a *perceptual-drifting hybrid loss* that combines instance-level alignment with distribution-level regularization. Our study further identifies a fully dual-stream architecture and RMS-based feature calibration as the preferred design choices.
- We show that these designs yield strong improvements on ImageNet-256 [10], outperforming the underlying pixel-space diffusion baseline (i.e., JiT [26]) as well as prior pixel-space diffusion methods.

2. Related Work

Pixel-space diffusion generation. Recent work has shown that, with suitable architectural and optimization choices, diffusion models trained directly in pixel space can approach latent diffusion performance [34]. JiT [26] demonstrates that competitive pixel-space generation is possible with a minimalist Transformer design, while Simple Diffusion [16], PixelDiT [48], and HDiT [7] improve training and scalability. Other methods add stronger inductive bi-

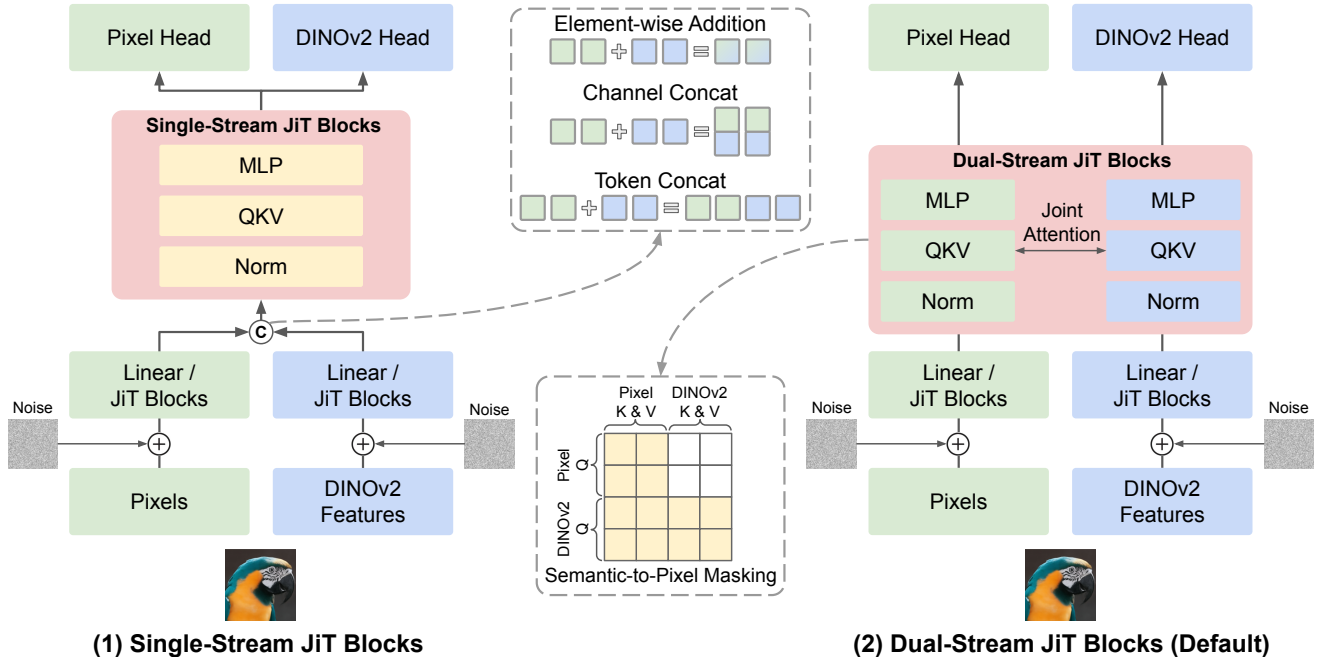


Figure 2. **Single-stream and dual-stream architectures for visual co-denoising.** In the *single-stream design* (left), noised pixels and DINOv2 features are fused after lightweight stream-specific preprocessing and then processed by shared JiT blocks. We study direct addition, channel concatenation, and token concatenation (see Sec. 3.2). In the *dual-stream design* (right), the two streams use separate normalization, MLP, and attention projections, while interacting through joint self-attention. A semantic-to-pixel attention mask is used to define the unconditional prediction for CFG (see Sec. 3.3). Both designs use separate output heads for pixel and DINOv2 prediction.

ases, such as decomposition in DeCo [30] and perceptual supervision in PixelGen [31]. We adopt pixel-space diffusion rather than VAE-latent diffusion because it avoids auto-encoder bottlenecks and learned latent-space biases, providing a cleaner setting for studying co-denoising and representation alignment.

Representation alignment for diffusion training. A growing line of work studies how pretrained visual representations can improve diffusion training. Recent analyses [35, 42] show that diffusion models learn meaningful internal features, but these are often weaker or less structured than those of strong self-supervised vision encoders. REPA [42] aligns intermediate diffusion features with pretrained representations such as DINOv2 [32], improving convergence and sample quality. Follow-up work studies which teacher properties matter most: iREPA [35] highlights spatial structure, while REPA-E [25] extends REPA-style supervision to end-to-end latent diffusion training with the VAE. Recent results also suggest that REPA-style alignment is most beneficial early in training and may over-constrain the representation space if applied too rigidly [42]. Motivated by this, we study representation alignment through co-denoising, compare auxiliary losses beyond REPA, and introduce a stronger hybrid alternative.

Visual co-denoising and joint generation across modal-

ities. Recent work has increasingly explored *joint denoising* or *joint generation* of multiple signals to improve information transfer, controllability, and structural consistency. In image generation, Latent Forcing [1] and ReDi [24] jointly model image latents and semantic features. In video generation, VideoJAM [4], UDPDiff [44], and UnityVideo [19] jointly generate video with structured signals such as segmentation, depth, or flow. Similar ideas extend to audio-visual generation [43], robotics and world modeling [2, 8, 9, 45, 52], and multimodal sequence modeling [14]. In contrast to these task-specific end-to-end designs, we provide a controlled study of visual co-denoising itself, isolating the architectural, guidance, loss, and calibration choices that make it effective and distilling them into a practical recipe for visual representation alignment.

3. A Closer Look at Visual Co-Denoising

In this section, we first formalize visual co-denoising in Sec. 3.1, then conduct a systematic study of the key design choices that govern its effectiveness, including model architecture (Sec. 3.2), unconditional prediction for CFG (Sec. 3.3), auxiliary training objectives (Sec. 3.4), and feature calibration via rescaling (Sec. 3.5). Starting from a standard pixel-space diffusion baseline (*e.g.*, JiT [26]), we use controlled ablations to isolate each component’s con-

tribution and derive a practical recipe, introducing *new designs tailored for visual co-denoising* along the way. Experiment setup details and additional ablations are deferred to Appendix Sec. A and Sec. B respectively.

3.1. Co-Denoising Formulation

We formalize visual co-denoising within a unified framework. Unlike standard pixel-space diffusion, which denoises only the image stream, co-denoising introduces an additional semantic feature stream from a pretrained visual encoder (*e.g.*, DINOv2 [32]). The core idea is to jointly denoise the pixel and semantic streams under a shared diffusion process, allowing the semantic stream to provide complementary supervision for semantically richer generation.

Unless otherwise specified, all experiments in this section follow the JiT [26] ablation protocol on ImageNet 256×256 [10], using a JiT-B/16 backbone trained for 200 epochs. We adopt the original JiT training configuration without additional hyperparameter tuning. Concretely, we extend the x -prediction and v -loss formulation of JiT to jointly denoise pixels and pretrained semantic features. Let x denote the clean image and d denote its encoded patch-level semantic features. We sample independent Gaussian noise $\epsilon_x, \epsilon_d \sim \mathcal{N}(\mathbf{0}, \mathbf{I})$ for the two streams. At diffusion time $t \in [0, 1]$, the corresponding noised inputs are

$$z_t^x = t x + (1-t) \epsilon_x, \quad z_t^d = t d + (1-t) \epsilon_d. \quad (1)$$

Given (z_t^x, z_t^d, t, c) , where c denotes the class condition, the co-denoising model jointly predicts the clean targets for the pixel and semantic streams:

$$(\hat{x}, \hat{d}) = f_\theta(z_t^x, z_t^d, t, c), \quad (2)$$

where f_θ denotes the co-denoising model, which could be implemented as either a shared-backbone or dual-stream architecture depending on the design variant. Following JiT, we convert these clean predictions into velocity predictions,

$$\hat{v}_x = (\hat{x} - z_t^x)/(1-t), \quad \hat{v}_d = (\hat{d} - z_t^d)/(1-t), \quad (3)$$

and supervise them with the ground-truth velocities,

$$v_x = x - \epsilon_x = (x - z_t^x)/(1-t) \quad (4)$$

$$v_d = d - \epsilon_d = (d - z_t^d)/(1-t). \quad (5)$$

The final objective is a weighted sum of the pixels and semantic features v -losses:

$$\mathcal{L}_{v\text{-co}} = \mathbb{E} \left[\|\hat{v}_x - v_x\|_2^2 + \lambda_d \|\hat{v}_d - v_d\|_2^2 \right], \quad (6)$$

where λ_d controls the weight of the semantic stream. This formulation provides a unified testbed for studying the effects of architecture, guidance, auxiliary losses, and feature calibration on representation alignment in co-denoising.

3.2. What Architecture Best Supports Visual Co-Denoising?

We begin by studying how semantic features should be integrated into a pixel-space diffusion backbone for co-denoising. Our goal is to identify the *architectural design that most effectively transfers information from pretrained semantic visual encoders to pixel features without limiting the expressiveness of the diffusion model*. To this end, we compare lightweight fusion within a largely shared backbone against more expressive designs that preserve feature-specific processing while enabling controlled cross-stream interaction. Fig. 2 illustrates the architectural variants, and Table 1 summarizes the corresponding results.

Baselines. We first report results for the original JiT-B/16 backbone [26] and a widened variant that increases the hidden dimension from 768 to 1088 to match the parameter count of the dual-stream models introduced later. We also include Latent Forcing [1] as a representative co-denoising baseline. For fair comparison, we keep the number of JiT blocks traversed by the pixel stream fixed across all variants, and maintain this setting throughout this subsection.

Single-stream variants. We consider a shared-backbone setting (Fig. 2, left) where pixel tokens x and semantic tokens d share most parameters. Within this setting, we compare three fusion strategies with model architectures derived from Latent Forcing [1]:

- **Direct Addition** (row (d)): Pixel tokens $x \in \mathbb{R}^{n \times d_1}$ and semantic features $d \in \mathbb{R}^{n \times d_2}$ are first projected into a shared hidden space $\mathbb{R}^{n \times d}$ via lightweight linear layers, then fused by *element-wise addition* and passed through shared JiT blocks. The pixel and semantic streams have two separate output heads. Our experiments in the main paper use $d_1 = d_2 = 768$ and a patch count of $n = 256$.
- **Channel-concatenation fusion** (row (e)): Pixel tokens x and semantic features d are concatenated along the channel dimension $\mathbb{R}^{n \times (d_1 + d_2)}$, and then linearly projected to the hidden dimension $\mathbb{R}^{n \times d}$ of JiT blocks.
- **Token-concatenation fusion** (rows (f-i)): Instead of concatenating along the channel dimension, we concatenate x and d along the sequence dimension $\mathbb{R}^{2n \times d}$ and input the combined token sequence into the JiT blocks.

Dual-stream variants. Motivated by the limitations of heavily shared backbones, we further introduce a *dual-stream* JiT architecture, illustrated on the right of Fig. 2, in which the pixel and semantic streams maintain separate normalization layers, MLPs, and attention projections (*i.e.*, Q/K/V), while interacting through joint self-attention. This design allows the model to adaptively determine *where* and *how* the two streams interact, while preserving dedicated processing pathways for each stream.

Analysis. As shown in Table 1, token-concatenation fusion outperforms direct addition and channel concatenation among the single-stream variants (rows (d)–(f)), suggesting

Table 1. **Comparison of architectural designs for visual co-denoising.** We compare baseline backbones, single-stream fusion strategies, and dual-stream fusion variants with different allocations of feature-specific and shared/dual-stream blocks. All variants keep the pixel stream depth fixed at 12 JiT blocks for fair comparison. JiT-B/16[‡] and JiT-B/16[†] denote widened variants with hidden dimensions increased from 768 to 1024 and 1088, respectively, to match the parameter counts of the dual-stream models. Blue rows mark the stronger variants used in subsequent analysis. Following previous works [1, 26], we mainly use FID as reference. We highlight the rows corresponding to the design with the best overall FID score in light blue.

Model	Backbone	#Params	#Feature-Specific Blocks	#Shared/Dual-Stream Blocks	CFG=1.0		
					FID↓	IS↑	
Baselines							
(a)	JiT-B/16 [26]	133M	-	-	32.54	49.5	
(b)	JiT-B/16 [26]	261M	-	-	22.67	69.9	
(c)	LatentForcing [1]	156M	2	10	13.06	102.2	
Single-Stream JiT Architecture							
(d)	DirectAddition	JiT-B/16	156M	2	10	15.15	103.4
(e)	ChannelConcat	JiT-B/16	157M	2	10	14.33	107.7
(f)	TokenConcat	JiT-B/16	156M	2	10	14.70	103.8
(g)	TokenConcat	JiT-B/16	177M	4	8	12.59	112.8
(h)	TokenConcat	JiT-B/16	198M	6	6	12.35	116.7
(i)	TokenConcat	JiT-B/16 [‡]	265M	6	6	9.74	129.45
Dual-Stream JiT Architecture							
(j)	TokenConcat	JiT-B/16	260M	6	6	11.78	115.4
(k)	TokenConcat	JiT-B/16	260M	4	8	11.40	118.3
(l)	TokenConcat	JiT-B/16	260M	2	10	10.24	124.5
(m)	TokenConcat	JiT-B/16	260M	0	12	8.86	132.8

that preserving feature-specific representations before interaction is preferable to early fusion in a shared space. Moreover, within token-concatenation, allocating more blocks to feature-specific processing consistently improves performance (rows (f)–(h)), indicating that excessive parameter sharing limits the model’s ability to preserve semantic information. Finally, among the dual-stream variants, the fully dual-stream architecture (row (m)) achieves the best FID of 8.86 under a comparable number of trainable parameters (row (i) and rows (j)–(l)), showing that allowing the model to *dynamically learn* cross-stream interaction at each block is more effective than imposing a fixed interaction pattern through a largely shared backbone. Therefore, we adopt the fully dual-stream architecture as the default model design in the remaining analysis. A more comprehensive comparison with additional single-stream variants is given in Table 7.

Finding 1: Effective visual feature alignment requires preserving feature-specific processing while enabling flexible cross-stream interaction. Token concatenation and a fully dual-stream model architecture emerge as the preferred designs.

3.3. How to Define Unconditional Prediction for CFG?

To enable classifier-free guidance (CFG), the model must define an unconditional prediction, *i.e.*, a prediction in

which the conditioning signals are removed. In our co-denoising setting, this is nontrivial because the model is conditioned on both class labels and semantic features. Guided sampling combines the conditional and unconditional predictions in the pixel and semantic streams as

$$\hat{v}_x = \hat{v}_x^{\text{uncond}} + s(\hat{v}_x^{\text{cond}} - \hat{v}_x^{\text{uncond}}) \quad (7)$$

$$\hat{v}_d = \hat{v}_d^{\text{uncond}} + s(\hat{v}_d^{\text{cond}} - \hat{v}_d^{\text{uncond}}) \quad (8)$$

where s denotes the CFG scale. Since guided generation depends critically on the quality of the unconditional branch, we next investigate *how to define an effective unconditional prediction for CFG in the co-denoising setting.*

Input-dropout baselines. Following prior work [1, 24], we first consider baseline unconditional predictions that drop conditioning inputs (semantic features and class labels) during training. Specifically, for semantic feature dropping, we use either (1) zeros or (2) a learnable [null] token to replace the semantic features. For each choice, we compare independent dropout of the class label and semantic features (rows (a)–(b)) against joint dropout (rows (e)–(f)).

Attention mask between pixel and semantic features. Beyond input-level dropout, we leverage the dual-stream architecture to define a *structurally unconditional* pathway. For unconditional samples, we apply *semantic-to-pixel masking* (see Fig. 3), which blocks cross-stream attention from the semantic stream to the pixel stream so that the pixel branch receives no semantic conditioning signal (rows

Table 2. **Comparison of unconditional prediction designs for classifier-free guidance under co-denoising.** We report unguided results at CFG= 1.0 and guided results at CFG= 2.9, which is the default guided evaluation setting in JiT [26]. We highlight the rows corresponding to the design with the best overall FID score in light blue .

Uncond. Type	Cond. Pred.	Uncond. Pred.	CFG=1.0		CFG=2.9	
			FID↓	IS↑	FID↓	IS↑
Independently Drop Labels & Semantic Features						
(a) Zero Embedding	$f_{\theta}([\mathbf{x}_t, \mathbf{d}_t], y, t)$	$f_{\theta}([\mathbf{x}_t, \mathbf{0}], \emptyset, t)$	9.17	126.3	6.69	165.6
(b) Learnable [null] Token	$f_{\theta}([\mathbf{x}_t, \mathbf{d}_t], y, t)$	$f_{\theta}([\mathbf{x}_t, [\text{null}]], \emptyset, t)$	9.37	126.7	6.64	165.7
(c) Bidirectional Cross-Stream Mask	$f_{\theta}([\mathbf{x}_t, \mathbf{d}_t], y, t)$	$f_{\theta}([\mathbf{x}_t, \mathbf{d}_t], \emptyset, t)$	11.08	101.9	7.17	143.5
(d) Semantic-to-Pixel Mask	$f_{\theta}([\mathbf{x}_t, \mathbf{d}_t], y, t)$	$f_{\theta}([\mathbf{x}_t, \mathbf{d}_t], \emptyset, t)$	7.28	136.8	3.59	189.6
Jointly Drop Labels & Semantic Features						
(e) Zero Embedding	$f_{\theta}([\mathbf{x}_t, \mathbf{d}_t], y, t)$	$f_{\theta}([\mathbf{x}_t, \mathbf{0}], \emptyset, t)$	15.58	98.8	24.75	82.4
(f) Learnable [null] Token	$f_{\theta}([\mathbf{x}_t, \mathbf{d}_t], y, t)$	$f_{\theta}([\mathbf{x}_t, [\text{null}]], \emptyset, t)$	10.80	118.3	25.2	88.3
(g) Bidirectional Cross-Stream Mask	$f_{\theta}([\mathbf{x}_t, \mathbf{d}_t], y, t)$	$f_{\theta}([\mathbf{x}_t, \mathbf{d}_t], \emptyset, t)$	7.53	129.1	5.66	173.6
(h) Semantic-to-Pixel Mask	$f_{\theta}([\mathbf{x}_t, \mathbf{d}_t], y, t)$	$f_{\theta}([\mathbf{x}_t, \mathbf{d}_t], \emptyset, t)$	5.62	158.5	3.18	219.4

(d) and (h)). We also study a symmetric variant, *bidirectional cross-stream masking*, which blocks attention in both directions (rows (c) and (g)). These variants test whether unconditional prediction is better defined via explicit control of information flow rather than input-level corruption.

Analysis. Table 2 first shows that under the baseline input-dropout strategy, independently dropping the class label and semantic features (rows (a)–(b)) performs substantially better than jointly dropping them (rows (e)–(f)). We hypothesize that jointly dropping both conditions makes the pixel-space guidance direction, $\Delta_x = \hat{v}_x^{\text{cond}} - \hat{v}_x^{\text{uncond}}$, a poorly calibrated estimate of the desired conditional guidance signal, which is then amplified by CFG scaling. In contrast, independent dropout exposes the model to partially conditioned cases and thus appears to improve the robustness of the learned guidance direction.

More importantly, explicitly defining the unconditional pathway through *structural* masking (rows (c)–(d)) is markedly more effective than input-level dropout (rows (a)–(b)) under independent dropout, suggesting that blocking semantic information from reaching the pixel branch yields a more reliable unconditional prediction. Among the structural variants, masking only the semantic-to-pixel pathway (row (d)) performs best, indicating that unconditional generation only requires removing semantic influence on the pixel output, while preserving the reverse pixel-to-semantic interaction remains beneficial. For structural masking, jointly dropping labels and semantic features (rows (g)–(h)) outperforms independent dropout (rows (c)–(d)), suggesting that once the unconditional branch is defined structurally, removing all conditioning sources during training better matches inference-time behavior.

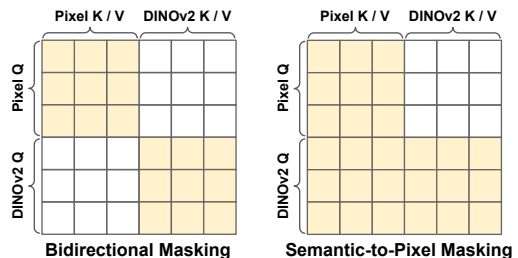


Figure 3. Comparison of two attention-masking strategies. Yellow tokens indicate the corresponding query and attended key/value tokens, while white tokens indicate positions whose attention scores are masked out.

Finding 2: For CFG under co-denoising, the most effective unconditional design is structural semantic-to-pixel masking with joint dropout of conditioning signals during training.

3.4. Which Auxiliary Loss Best Improves Co-Denoising?

The default V-Co objective in Eq. (6) supervises both streams through the co-denoising v -loss, but it mainly enforces local target matching and may not fully capture higher-level semantic alignment. We therefore study *which auxiliary objectives provide the most effective complementary supervision in representation space*, and ultimately design a hybrid loss that better combines their strengths.

Balancing pixel and semantic losses. Before exploring additional auxiliary objectives, we first tune the relative weight of the semantic-stream loss through λ_d in Eq. (6). As shown in Fig. 4, $\lambda_d \in \{0.01, 0.1\}$ gives the best FID. Under these settings, the average parameter-gradient norm in the pixel branch is approximately $4\times$ and $2\times$ that of the

Table 3. **Comparison of auxiliary losses applied to V-Co.** We report unguided results at CFG= 1.0 and guided results at the best CFG selected from a sweep over [1.5, 5.5] for each method (2.5 for (a) REPA loss, 2.1 for (b) perceptual loss, 2.4 for (c) drifting loss, and 2.0 for (d) the perceptual-drifting hybrid loss). All results here are obtained after 300 epochs of training. We highlight the row with the best guided FID score in light blue .

Aux. Loss Type	Unguided (CFG=1.0)		Guided (Best CFG> 1.0)	
	FID↓	IS↑	FID↓	IS↑
Baseline: V-Co w/ default V-Pred Loss	5.38	153.6	2.96	206.6
(a) V-Co + REPA Loss	5.63	149.4	2.91 (0.05 ↓)	202.8
(b) V-Co + Perceptual Loss	4.28	177.6	2.73 (0.23 ↓)	228.5
(c) V-Co + Drifting Loss	4.86	164.3	2.85 (0.11 ↓)	211.5
(d) V-Co + Perceptual-Drifting Hybrid Loss	4.44	189.0	2.44 (0.52 ↓)	249.9

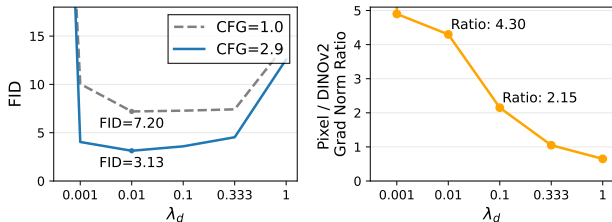


Figure 4. Influence of the DINO diffusion loss coefficient λ_d . See Sec. 3.4 for details.

semantic branch, respectively. This suggests that semantic supervision is most effective when it provides meaningful guidance while remaining secondary to the primary pixel-space objective.

REPA loss [25]. On top of the co-denoising objective, we further consider a REPA-style representation alignment loss on the pixel branch. Concretely, let h_ℓ^x denote the intermediate hidden representation of the pixel branch at layer ℓ . We align this hidden state to the representation of the ground-truth image \mathbf{x} extracted by a frozen pretrained DINOv2 visual encoder $\phi(\cdot)$. The auxiliary objective is defined as $\mathcal{L}_{\text{REPA}} = \|g(h_\ell^x) - \phi(\mathbf{x})\|_2^2$, where $g(\cdot)$ denotes a lightweight MLP projector used to map the intermediate hidden state to the encoder feature space. Empirically, we find that applying the REPA loss to the fourth block in JiT-Base yields the best performance, consistent with the configuration used in the original REPA paper, which adopts SiT-Base [29] as the backbone.

Perceptual loss in semantic feature space. We also consider a perceptual loss [21, 31] in the pretrained semantic feature space. Given the predicted clean image $\hat{\mathbf{x}}$ and the ground-truth image \mathbf{x} , we extract their features using a frozen pretrained DINOv2 encoder $\phi(\cdot)$ and minimize their discrepancy: $\mathcal{L}_{\text{perc}} = \|\phi(\hat{\mathbf{x}}) - \phi(\mathbf{x})\|_2^2$. Unlike REPA, which aligns intermediate hidden states, this loss directly supervises the predicted image in semantic feature space.

Drifting loss in semantic feature space. Drifting loss [11]

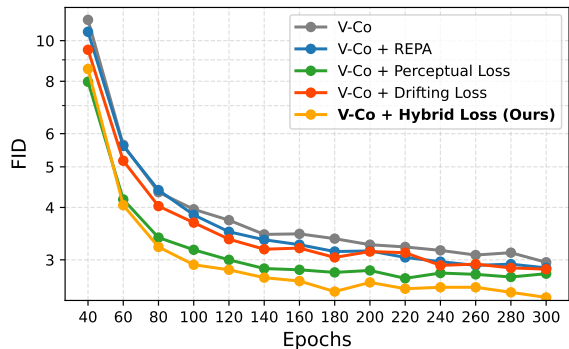


Figure 5. Comparison of guided FID (*i.e.*, FID computed from samples generated with CFG).

was recently proposed for single-step image generation to move the generated distribution toward the real one. Unlike diffusion v -prediction, REPA, and perceptual losses, which impose pairwise supervision between generated and real samples, drifting loss operates at the distribution level. To study its effectiveness in multi-step diffusion, we implement it in DINO feature space. Let $\phi(\cdot)$ denote a frozen DINOv2 encoder, let $\hat{\mathbf{x}}$ be the predicted clean image from the pixel branch, and define $\mathbf{u} = \phi(\hat{\mathbf{x}})$. We construct a drifting field as follows:

$$V(\mathbf{u}) = V^+(\mathbf{u}) - V^-(\mathbf{u}), \quad (9)$$

$$V^+(\mathbf{u}) = \frac{1}{Z_+(\mathbf{u})} \mathbb{E}_{\mathbf{x}^+ \sim p_{\text{data}}} [k(\mathbf{u}, \phi(\mathbf{x}^+))(\phi(\mathbf{x}^+) - \mathbf{u})], \quad (10)$$

$$V^-(\mathbf{u}) = \frac{1}{Z_-(\mathbf{u})} \mathbb{E}_{\mathbf{x}^- \sim p_{\text{gen}}} [k(\mathbf{u}, \phi(\mathbf{x}^-))(\phi(\mathbf{x}^-) - \mathbf{u})], \quad (11)$$

where p_{data} and p_{gen} denote the real and generated image distributions respectively. $k(\mathbf{a}, \mathbf{b}) = \exp(-\|\mathbf{a} - \mathbf{b}\|_2^2 / \tau)$ is a similarity kernel and Z_+ , Z_- normalize the kernel weights. The drifting loss is defined as $\mathcal{L}_{\text{drift}} = \|\mathbf{u} - \text{sg}(\mathbf{u} + V(\mathbf{u}))\|_2^2$, where $\text{sg}(\cdot)$ denotes stop-gradient.

Table 4. **Feature rescaling vs. noise-schedule shifting in V-Co.** We compare our default V-Co model with RMS scaling against variants *without RMS scaling* and *with noise-schedule shifting*. We report unguided results at CFG= 1.0 and guided results at the best CFG selected from a sweep over [1.5, 5.5] for each method. We highlight the row with the best guided FID score in light blue .

Model	Unguided (CFG=1.0)		Guided (Best CFG> 1.0)	
	FID↓	IS↑	FID↓	IS↑
(a) V-Co w/o rms scaling	9.12	188.6	5.28	150.4
(b) V-Co w/o rms scaling + noise schedule shifting	4.81	205.6	2.93	272.4
(c) V-Co w/ rms scaling (default)	5.38	177.0	2.52	242.6

Perceptual-Drifting Hybrid loss. Perceptual loss and drifting loss provide two complementary forms of supervision. Perceptual loss encourages *instance-level* semantic fidelity by pulling each generated image toward the semantic feature of its paired ground-truth target, while drifting loss promotes *distributional coverage* by discouraging generated features from collapsing toward dense regions of the generated distribution. Motivated by this complementarity, we propose a hybrid objective that formulates perceptual alignment as a positive vector field and drifting-based repulsion as a negative correction.

Unlike the original drifting loss, we replace its positive real-distribution term with the current sample’s *paired perceptual field* while retaining the generated-distribution term as a negative correction. This is better suited to multi-step denoising, where each noisy input is paired with a specific ground-truth image.

Specifically, we define the positive perceptual field as:

$$V^+(\mathbf{u}_i) = \phi(\mathbf{x}_i) - \phi(\hat{\mathbf{x}}_i), \quad (12)$$

which pulls the generated sample toward the semantic feature of its paired ground-truth target. The negative field computes repulsion from nearby generated samples within the same class. For each sample i , we compute normalized kernel weights over other samples $j \neq i$ of the same class:

$$\alpha_{ij} = \frac{\exp(-\|\phi(\hat{\mathbf{x}}_i) - \phi(\hat{\mathbf{x}}_j)\|^2/\tau_{\text{rep}})}{\sum_{k \neq i} \exp(-\|\phi(\hat{\mathbf{x}}_i) - \phi(\hat{\mathbf{x}}_k)\|^2/\tau_{\text{rep}})}, \quad (13)$$

where τ_{rep} is the repulsion temperature. Note that $\sum_{j \neq i} \alpha_{ij} = 1$. The repulsion direction points from sample i toward the weighted centroid of its neighbors:

$$V^-(\mathbf{u}_i) = \sum_{j \neq i} \alpha_{ij} \phi(\hat{\mathbf{x}}_j) - \phi(\hat{\mathbf{x}}_i). \quad (14)$$

To adaptively balance attraction and repulsion, we introduce a *similarity-based gating* mechanism based on how close the generated feature is to its target:

$$s_i = \exp\left(-\frac{\|\phi(\hat{\mathbf{x}}_i) - \phi(\mathbf{x}_i)\|^2}{\tau_{\text{gate}}}\right), \quad (15)$$

where τ_{gate} is a temperature parameter controlling the sensitivity of the gate. We then combine the two fields into a hybrid field:

$$V_{\text{hyb}}(\mathbf{u}_i) = s_i \cdot V^+(\mathbf{u}_i) - (1 - s_i) \cdot V^-(\mathbf{u}_i). \quad (16)$$

Intuitively, when the generated feature is far from the target ($s_i \approx 0$), repulsion dominates to prevent mode collapse; when the generated feature is close to the target ($s_i \approx 1$), pure attraction ensures clean convergence.

The final objective is:

$$\mathcal{L} = \mathcal{L}_{\text{v-co}} + \lambda_{\text{hyb}} \mathcal{L}_{\text{hyb}} \quad (17)$$

$$= \mathcal{L}_{\text{v-co}} + \lambda_{\text{hyb}} \|\mathbf{u}_i - \text{sg}(\mathbf{u}_i + V_{\text{hyb}}(\mathbf{u}_i))\|_2^2. \quad (18)$$

Analysis. Table 3 and Fig. 5 quantify the impact of different auxiliary objectives on co-denoising. REPA provides only a marginal guided improvement over the default V-Co objective (FID 2.91 vs. 2.96 for CFG> 1), suggesting limited benefit from intermediate alignment and potential constraints on model’s expressiveness [42]. Perceptual loss yields a larger gain (FID 2.73), indicating effective instance-level semantic alignment, while drifting loss provides a smaller improvement (FID 2.85) but contributes distribution-level supervision. Combining these complementary signals, our hybrid objective achieves the best guided result (FID 2.44), suggesting that instance-level alignment is most effective when paired with explicit distribution-level correction.

Finding 3: For visual co-denoising, auxiliary losses work best when combining instance-level alignment with distribution-level regularization.

3.5. How Should Semantic Features Be Calibrated for Co-Denoising?

Before concluding the recipe, we consider *how to calibrate the semantic stream relative to the pixel stream during co-denoising*. Since the two inputs lie in different representation spaces and can have very different signal scales, applying the same diffusion timestep to both streams may result in mismatched denoising difficulty and thus imbalanced

Table 5. **Reference results on ImageNet 256×256.** FID and IS of 50K samples are evaluated. The “pre-training” columns list the external models required to obtain the results. The #Params column reports the parameter count of the denoising model and the decoder (if used). Following previous works [1, 26], we mainly use FID as reference.

ImageNet 256 × 256	Pre-training		#Params	#Epochs	FID↓	IS↑
	Tokenizer	SSL Encoder				
Latent-space Diffusion						
DiT-XL/2 [33]	SD-VAE	-	675+49M	1400	2.27	278.2
SiT-XL/2 [29]	SD-VAE	-	675+49M	1400	2.06	277.5
REPA [42], SiT-XL/2	SD-VAE	DINOv2	675+49M	800	1.42	305.7
LightningDiT-XL/2 [46]	VA-VAE	DINOv2	675+49M	800	1.35	295.3
DDT-XL/2 [41]	SD-VAE	DINOv2	675+49M	400	1.26	310.6
RAE [50], DiT ^{DH} -XL/2	RAE	DINOv2	839+415M	800	1.13	262.6
Pixel-space (non-diffusion)						
JetFormer [38]	-	-	2.8B	-	6.64	-
FractalMAR-H [27]	-	-	848M	600	6.15	348.9
Pixel-space Diffusion						
ADM-G [12]	-	-	554M	400	4.59	186.7
RIN [20]	-	-	410M	-	3.42	182.0
SiD [16], UViT/2	-	-	2B	800	2.44	256.3
VDM++, UViT/2	-	-	2B	800	2.12	267.7
SiD2 [17], UViT/2	-	-	N/A	-	1.73	-
SiD2 [17], UViT/1	-	-	N/A	-	1.38	-
PixelFlow [5], XL/4	-	-	677M	320	1.98	282.1
PixNerd [40], XL/16	-	DINOv2	700M	160	2.15	297.0
DeCo-XL/16 [30]	-	DINOv2	682M	600	1.69	304.0
PixelGen-XL/16 [31]	-	DINOv2	676M	160	1.83	293.6
ReDi [24], SiT-XL/2	-	DINOv2	675M	350	1.72	278.7
ReDi [24], SiT-XL/2	-	DINOv2	675M	800	1.61	295.1
Latent Forcing [1], JiT-B/16	-	DINOv2	465M	200	2.48	-
JiT-B/16 [26]	-	-	131M	600	3.66	275.1
JiT-L/16 [26]	-	-	459M	600	2.36	298.5
JiT-H/16 [26]	-	-	953M	600	1.86	303.4
JiT-G/16 [26]	-	-	2B	600	1.82	292.6
V-Co-B/16	-	DINOv2	260M	200	2.52	242.6
V-Co-L/16	-	DINOv2	918M	200	2.10	243.0
V-Co-H/16	-	DINOv2	1.9B	200	1.85	246.5
V-Co-B/16	-	DINOv2	260M	600	2.33	250.1
V-Co-L/16	-	DINOv2	918M	500	1.72	245.3
V-Co-H/16	-	DINOv2	1.9B	300	1.71	263.3

optimization. Related co-denoising work has addressed this issue by shifting the semantic-stream diffusion schedule [1]. Here, we study two natural calibration strategies: rescaling the semantic features to match the pixel-space signal level, or equivalently shifting the semantic-stream diffusion schedule. As we show below, the two can be formulated to achieve the same signal-to-noise ratio (SNR).

SNR matching via feature rescaling. As defined in Eq. (1), pixels and semantic features share the same timestep $t \in [0, 1]$. Under this flow-matching parameteri-

zation, the noised input takes the form

$$z_t = t s + (1 - t) \epsilon, \quad (19)$$

where s denotes the clean signal and $\epsilon \sim \mathcal{N}(\mathbf{0}, \mathbf{I})$ is the injected noise. We define the signal-to-noise ratio (SNR) at time t as the ratio between the signal power and the noise power:

$$\text{SNR}(t) = \frac{\mathbb{E}\|t s\|^2}{\mathbb{E}\|(1-t)\epsilon\|^2} = \frac{t^2 \mathbb{E}\|s\|^2}{(1-t)^2 \mathbb{E}\|\epsilon\|^2}. \quad (20)$$

Since t is shared across streams and the noise scale is fixed, matching denoising difficulty reduces to matching signal

magnitude. Let \mathbf{d} denote the original semantic feature and \mathbf{d}' its rescaled version. We therefore rescale the semantic features as

$$\mathbf{d}' = \alpha \mathbf{d}, \quad \alpha = \frac{\sqrt{\mathbb{E}[\mathbf{x}^2]}}{\sqrt{\mathbb{E}[\mathbf{d}^2]}}, \quad (21)$$

so that the semantic features have the same RMS magnitude as the pixel signal.

Equivalent SNR matching via timestep shifting. Equivalently, one can keep the semantic feature \mathbf{d} fixed and instead shift its timestep from t to t' such that $\text{SNR}_{\mathbf{d}}(t') = \text{SNR}_{\mathbf{d}'}(t)$. Using Eq. (20), this gives $\frac{t'}{1-t'} = \alpha \frac{t}{1-t}$, and

$$t' = \frac{\alpha t}{1 + (\alpha - 1)t}. \quad (22)$$

Therefore, rescaling the semantic features by α is SNR-equivalent to applying a shifted diffusion schedule to the unscaled semantic stream.

Analysis. In Table 4, we compare our default V-Co model against variants *without RMS scaling* and *with noise-schedule shifting* in place of RMS scaling. Removing RMS scaling substantially worsens performance relative to our default setting (guided FID: 5.28 vs. 2.52). Replacing RMS scaling with noise-schedule shifting gives broadly comparable overall results, but yields worse guided FID (2.93 vs. 2.52), consistent with the SNR-based equivalence discussed above. In practice, we adopt RMS-based feature scaling because of its simplicity and strong performance.

Finding 4: Effective co-denoising requires calibrating the semantic and pixel streams to comparable denoising difficulty. RMS-based feature rescaling provides a simple and practical solution.

4. Full Recipe and SoTA Comparison

We combine the best-performing ablation choices into a practical visual co-denoising (**V-Co**) recipe: a fully dual-stream JiT backbone (Sec. 3.2), structural semantic-to-pixel masking with joint dropout for CFG (Sec. 3.3), a perceptual-drifting hybrid loss (Sec. 3.4), and RMS-based feature rescaling (Sec. 3.5). These components are complementary: the architecture determines *where* streams interact, masking defines *how* guidance is formed, the hybrid loss specifies *what* semantic supervision to apply, and RMS scaling matches denoising difficulty.

We next evaluate this full recipe against prior SoTA methods on ImageNet [10] 256×256 , including latent-space diffusion models, and pixel-space methods. As shown in Table 5, V-Co achieves strong performance among pixel-space diffusion models. Notably, V-Co-B/16 with only 260M parameters, matches JiT-L/16 with 459M parameters

(FID 2.33 vs. 2.36). V-Co-L/16 and V-Co-H/16, trained for 500 and 300 epochs respectively, outperform JiT-G/16 with 2B parameters (FID 1.71 vs. 1.82) and other strong pixel-diffusion methods. In addition, our method with simple RMS scaling matches or outperforms Latent Forcing [1], which relies on separate noise schedules for pixels and DI-NOv2 features. These results demonstrate that a carefully designed co-denoising recipe is both effective and scalable for representation-aligned pixel-space generation.

5. Conclusion

We presented V-Co, a visual co-denoising framework for representation-aligned pixel-space generation. We identify four key ingredients for effective co-denoising: a fully dual-stream backbone, structural semantic-to-pixel masking for classifier-free guidance, a perceptual-drifting hybrid loss, and RMS-based feature rescaling. Together, they form a simple and scalable recipe that improves semantic alignment and generative quality, with strong ImageNet results and clear scalability with model size and training duration. We hope this work can inspire future research on co-denoising and representation-aligned generative modeling.

6. Acknowledgments

This work was supported by ONR Grant N00014-23-1-2356, ARO Award W911NF2110220, DARPA ECOLE Program No. HR00112390060, and NSF-AI Engage Institute DRL-2112635. The views contained in this article are those of the authors and not of the funding agency.

References

- [1] Alan Baade, Eric Ryan Chan, Kyle Sargent, Changan Chen, Justin Johnson, Ehsan Adeli, and Li Fei-Fei. Latent forcing: Reordering the diffusion trajectory for pixel-space image generation. *arXiv preprint arXiv:2602.11401*, 2026. 2, 3, 4, 5, 9, 10, 14
- [2] Hongzhe Bi, Hengkai Tan, Shenghao Xie, Zeyuan Wang, Shuhe Huang, Haitian Liu, Ruowen Zhao, Yao Feng, Chendong Xiang, Yinze Rong, et al. Motus: A unified latent action world model. *arXiv preprint arXiv:2512.13030*, 2025. 2, 3
- [3] Hun Chang, Byunghee Cha, and Jong Chul Ye. Dino-sae: Dino spherical autoencoder for high-fidelity image reconstruction and generation. *arXiv preprint arXiv:2601.22904*, 2026. 2
- [4] Hila Chefer, Uriel Singer, Amit Zohar, Yuval Kirstain, Adam Polyak, Yaniv Taigman, Lior Wolf, and Shelly Sheynin. Videojam: Joint appearance-motion representations for enhanced motion generation in video models. In *Forty-second International Conference on Machine Learning*, 2025. 2, 3
- [5] Shoufa Chen, Chongjian Ge, Shilong Zhang, Peize Sun, and Ping Luo. Pixelflow: Pixel-space generative models with flow. *arXiv preprint arXiv:2504.07963*, 2025. 9

- [6] Zhennan Chen, Junwei Zhu, Xu Chen, Jiangning Zhang, Xiaobin Hu, Hanzhen Zhao, Chengjie Wang, Jian Yang, and Ying Tai. Dip: Taming diffusion models in pixel space. *arXiv preprint arXiv:2511.18822*, 2025. 1
- [7] Katherine Crowson, Stefan Andreas Baumann, Alex Birch, Tanishq Mathew Abraham, Daniel Z Kaplan, and Enrico Shippole. Scalable high-resolution pixel-space image synthesis with hourglass diffusion transformers. In *Forty-first International Conference on Machine Learning*, 2024. 2
- [8] Lingwei Dang, Zonghan Li, Juntong Li, Hongwen Zhang, Liang An, Yebin Liu, and Qingyao Wu. Syncmv4d: Synchronized multi-view joint diffusion of appearance and motion for hand-object interaction synthesis. *arXiv preprint arXiv:2511.19319*, 2025. 2, 3
- [9] Lingwei Dang, Ruizhi Shao, Hongwen Zhang, Wei MIN, Yebin Liu, and Qingyao Wu. Svimo: Synchronized diffusion for video and motion generation in hand-object interaction scenarios. In *The Thirty-ninth Annual Conference on Neural Information Processing Systems*, 2025. 2, 3
- [10] Jia Deng, Wei Dong, Richard Socher, Li-Jia Li, Kai Li, and Li Fei-Fei. Imagenet: A large-scale hierarchical image database. In *2009 IEEE conference on computer vision and pattern recognition*, pages 248–255. Ieee, 2009. 2, 4, 10
- [11] Mingyang Deng, He Li, Tianhong Li, Yilun Du, and Kaiming He. Generative modeling via drifting. *arXiv preprint arXiv:2602.04770*, 2026. 7
- [12] Prafulla Dhariwal and Alexander Nichol. Diffusion models beat gans on image synthesis. *Advances in neural information processing systems*, 34:8780–8794, 2021. 9
- [13] Patrick Esser, Sumith Kulal, Andreas Blattmann, Rahim Entezari, Jonas Müller, Harry Saini, Yam Levi, Dominik Lorenz, Axel Sauer, Frederic Boesel, et al. Scaling rectified flow transformers for high-resolution image synthesis. In *Forty-first international conference on machine learning*, 2024. 1
- [14] Xiaochuang Han, Youssef Emad, Melissa Hall, John Nguyen, Karthik Padthe, Liam Robbins, Amir Bar, Delong Chen, Michal Drozdal, Maha Elbayad, et al. Tv2tv: A unified framework for interleaved language and video generation. *arXiv preprint arXiv:2512.05103*, 2025. 2, 3
- [15] Karl Heun et al. Neue methoden zur approximativen integration der differentialgleichungen einer unabhängigen veränderlichen. *Z. Math. Phys*, 45(23-38):7, 1900. 13
- [16] Emiel Hoogeboom, Jonathan Heek, and Tim Salimans. simple diffusion: End-to-end diffusion for high resolution images. In *International Conference on Machine Learning*, pages 13213–13232. PMLR, 2023. 2, 9
- [17] Emiel Hoogeboom, Thomas Mensink, Jonathan Heek, Kay Lamerigts, Ruiqi Gao, and Tim Salimans. Simpler diffusion: 1.5 fid on imagenet512 with pixel-space diffusion. In *Proceedings of the Computer Vision and Pattern Recognition Conference*, pages 18062–18071, 2025. 9
- [18] Zheyuan Hu, Chieh-Hsin Lai, Ge Wu, Yuki Mitsufuji, and Stefano Ermon. Meanflow transformers with representation autoencoders. *arXiv preprint arXiv:2511.13019*, 2025. 2
- [19] Jiehui Huang, Yuechen Zhang, Xu He, Yuan Gao, Zhi Cen, Bin Xia, Yan Zhou, Xin Tao, Pengfei Wan, and Jiaya Jia. Unityvideo: Unified multi-modal multi-task learning for enhancing world-aware video generation. *arXiv preprint arXiv:2512.07831*, 2025. 2, 3
- [20] Allan Jabri, David J Fleet, and Ting Chen. Scalable adaptive computation for iterative generation. In *International Conference on Machine Learning*, pages 14569–14589. PMLR, 2023. 9
- [21] Justin Johnson, Alexandre Alahi, and Li Fei-Fei. Perceptual losses for real-time style transfer and super-resolution. In *European conference on computer vision*, pages 694–711. Springer, 2016. 7
- [22] Diederik P Kingma and Jimmy Ba. Adam: A method for stochastic optimization. *arXiv preprint arXiv:1412.6980*, 2014. 13
- [23] Diederik P Kingma and Max Welling. Auto-encoding variational bayes. *arXiv preprint arXiv:1312.6114*, 2013. 1
- [24] Theodoros Kouzelis, Efstathios Karypidis, Ioannis Kakogeorgiou, Spyros Gidaris, and Nikos Komodakis. Boosting generative image modeling via joint image-feature synthesis. In *The Thirty-ninth Annual Conference on Neural Information Processing Systems*, 2025. 2, 3, 5, 9
- [25] Xingjian Leng, Jaskirat Singh, Yunzhong Hou, Zhenchang Xing, Saining Xie, and Liang Zheng. Repa-e: Unlocking vae for end-to-end tuning of latent diffusion transformers. In *Proceedings of the IEEE/CVF International Conference on Computer Vision*, pages 18262–18272, 2025. 3, 7
- [26] Tianhong Li and Kaiming He. Back to basics: Let denoising generative models denoise. *arXiv preprint arXiv:2511.13720*, 2025. 1, 2, 3, 4, 5, 6, 9, 13, 14
- [27] Tianhong Li, Qinyi Sun, Lijie Fan, and Kaiming He. Fractal generative models. *arXiv preprint arXiv:2502.17437*, 2025. 9
- [28] Yiyang Lu, Susie Lu, Qiao Sun, Hanhong Zhao, Zhicheng Jiang, Xianbang Wang, Tianhong Li, Zhengyang Geng, and Kaiming He. One-step latent-free image generation with pixel mean flows. *arXiv preprint arXiv:2601.22158*, 2026. 1
- [29] Nanye Ma, Mark Goldstein, Michael S Albergo, Nicholas M Boffi, Eric Vanden-Eijnden, and Saining Xie. Sit: Exploring flow and diffusion-based generative models with scalable interpolant transformers. In *European Conference on Computer Vision*, pages 23–40. Springer, 2024. 1, 7, 9
- [30] Zehong Ma, Longhui Wei, Shuai Wang, Shiliang Zhang, and Qi Tian. Deco: Frequency-decoupled pixel diffusion for end-to-end image generation. *arXiv preprint arXiv:2511.19365*, 2025. 3, 9
- [31] Zehong Ma, Ruihan Xu, and Shiliang Zhang. Pixelgen: Pixel diffusion beats latent diffusion with perceptual loss. *arXiv preprint arXiv:2602.02493*, 2026. 1, 3, 7, 9
- [32] Maxime Oquab, Timothée Darcet, Théo Moutakanni, Huy Vo, Marc Szafraniec, Vasil Khalidov, Pierre Fernandez, Daniel Haziza, Francisco Massa, Alaaeldin El-Nouby, et al. Dinov2: Learning robust visual features without supervision. *arXiv preprint arXiv:2304.07193*, 2023. 2, 3, 4, 13
- [33] William Peebles and Saining Xie. Scalable diffusion models with transformers. In *Proceedings of the IEEE/CVF international conference on computer vision*, pages 4195–4205, 2023. 1, 9

- [34] Robin Rombach, Andreas Blattmann, Dominik Lorenz, Patrick Esser, and Björn Ommer. High-resolution image synthesis with latent diffusion models. In *Proceedings of the IEEE/CVF Conference on Computer Vision and Pattern Recognition (CVPR)*, pages 10684–10695, 2022. 1, 2
- [35] Jaskirat Singh, Xingjian Leng, Zongze Wu, Liang Zheng, Richard Zhang, Eli Shechtman, and Saining Xie. What Matters for Representation Alignment: Global Information or Spatial Structure? *arXiv preprint arXiv:2512.10794*, 2025. 2, 3, 16
- [36] Yuchuan Tian, Hanting Chen, Mengyu Zheng, Yuchen Liang, Chao Xu, and Yunhe Wang. U-repa: Aligning diffusion u-nets to vits. *arXiv preprint arXiv:2503.18414*, 2025. 2
- [37] Shengbang Tong, Boyang Zheng, Ziteng Wang, Bingda Tang, Nanye Ma, Ellis Brown, Jihan Yang, Rob Fergus, Yann LeCun, and Saining Xie. Scaling text-to-image diffusion transformers with representation autoencoders. *arXiv preprint arXiv:2601.16208*, 2026. 2
- [38] Michael Tschannen, André Susano Pinto, and Alexander Kolesnikov. Jetformer: An autoregressive generative model of raw images and text. In *The Thirteenth International Conference on Learning Representations*, 2025. 9
- [39] Mengmeng Wang, Dengyang Jiang, Liuzhuozheng Li, Yucheng Lin, Guojiang Shen, Xiangjie Kong, Yong Liu, Guang Dai, and Jingdong Wang. Vae-repa: Variational autoencoder representation alignment for efficient diffusion training. *arXiv preprint arXiv:2601.17830*, 2026. 2
- [40] Shuai Wang, Ziteng Gao, Chenhui Zhu, Weilin Huang, and Limin Wang. Pixnerd: Pixel neural field diffusion. *arXiv preprint arXiv:2507.23268*, 2025. 9
- [41] Shuai Wang, Zhi Tian, Weilin Huang, and Limin Wang. Ddt: Decoupled diffusion transformer. *arXiv preprint arXiv:2504.05741*, 2025. 9
- [42] Ziqiao Wang, Wangbo Zhao, Yuhao Zhou, Zekai Li, Zhiyuan Liang, Mingjia Shi, Xuanlei Zhao, Pengfei Zhou, Kaipeng Zhang, Zhangyang Wang, et al. Repa works until it doesn't: Early-stopped, holistic alignment supercharges diffusion training. *arXiv preprint arXiv:2505.16792*, 2025. 2, 3, 8, 9
- [43] Jianzong Wu, Hao Lian, Dachao Hao, Ye Tian, Qingyu Shi, Biaocong Chen, Hao Jiang, and Yunhai Tong. Does hearing help seeing? investigating audio-video joint denoising for video generation. *arXiv preprint arXiv:2512.02457*, 2025. 2, 3
- [44] Lehan Yang, Lu Qi, Xiangtai Li, Sheng Li, Varun Jampani, and Ming-Hsuan Yang. Unified dense prediction of video diffusion. In *Proceedings of the Computer Vision and Pattern Recognition Conference*, pages 28963–28973, 2025. 3
- [45] Yuxiao Yang, Hualian Sheng, Sijia Cai, Jing Lin, Jiahao Wang, Bing Deng, Junzhe Lu, Haoqian Wang, and Jieping Ye. Echomotion: Unified human video and motion generation via dual-modality diffusion transformer. *arXiv preprint arXiv:2512.18814*, 2025. 2, 3
- [46] Jingfeng Yao, Bin Yang, and Xinggong Wang. Reconstruction vs. generation: Taming optimization dilemma in latent diffusion models. In *Proceedings of the IEEE/CVF Conference on Computer Vision and Pattern Recognition*, 2025. 9
- [47] Sihyun Yu, Sangkyung Kwak, Huiwon Jang, Jongheon Jeong, Jonathan Huang, Jinwoo Shin, and Saining Xie. Representation alignment for generation: Training diffusion transformers is easier than you think. In *The Thirteenth International Conference on Learning Representations*, 2025. 16
- [48] Yongsheng Yu, Wei Xiong, Weili Nie, Yichen Sheng, Shiqiu Liu, and Jiebo Luo. Pixeldit: Pixel diffusion transformers for image generation. *arXiv preprint arXiv:2511.20645*, 2025. 1, 2
- [49] Xiangdong Zhang, Jiaqi Liao, Shaofeng Zhang, Fanqing Meng, Xiangpeng Wan, Junchi Yan, and Yu Cheng. Videorepa: Learning physics for video generation through relational alignment with foundation models. *arXiv preprint arXiv:2505.23656*, 2025. 2
- [50] Boyang Zheng, Nanye Ma, Shengbang Tong, and Saining Xie. Diffusion transformers with representation autoencoders. *arXiv preprint arXiv:2510.11690*, 2025. 2, 9, 13, 16
- [51] Ruijie Zheng, Jing Wang, Scott Reed, Johan Bjorck, Yu Fang, Fengyuan Hu, Joel Jang, Kaushil Kundalia, Zongyu Lin, Loic Magne, et al. Flare: Robot learning with implicit world modeling. *arXiv preprint arXiv:2505.15659*, 2025. 2
- [52] Zhide Zhong, Haodong Yan, Junfeng Li, Xiangchen Liu, Xin Gong, Tianran Zhang, Wenxuan Song, Jiayi Chen, Xinhua Zheng, Hesheng Wang, et al. Flowvla: Visual chain of thought-based motion reasoning for vision-language-action models. *arXiv preprint arXiv:2508.18269*, 2025. 2, 3

Appendix

A. Experiment Setup Details

We report the hyper-parameters of the final model used for evaluation in Table 6. Throughout Sec. 3, these design choices are introduced progressively and tuned step by step toward the final configuration.

Table 6. **Configurations of experiments.** Architecture, feature pre-processing, training, and sampling settings for V-Co-B/L/H. We color the newly added hyper-parameters on top of JIT [26] codebase in light blue .

	V-Co-B	V-Co-L	V-Co-H
Architecture			
Depth	12	24	32
Hidden dim	768	1024	1280
Heads	12	16	16
Image size		256	
Patch size		16	
Bottleneck	128	128	256
Dropout		0	
In-context class tokens		32 (if used)	
In-context start block	4	8	10
Feature Pre-Processing			
Pixels	[−1, 1] linear min-max rescaling		
DINOv2	Patch-level scaling following RAE [50]		
Training			
Epochs	200 (ablation), 600		
Warmup epochs [26]	5		
Optimizer	Adam [22], $\beta_1, \beta_2 = 0.9, 0.95$		
Batch size	1024		
Learning rate	$2e-4$		
LR schedule	constant		
Weight decay	0		
EMA decay	{0.9996, 0.9998, 0.9999}		
Time sampler	$\text{logit}(t) \sim \mathcal{N}(\mu, \sigma^2)$, $\mu = -0.8$, $\sigma = 0.8$		
Noise scale	1.0		
Clip of $(1 - t)$ in division	0.05		
Class & DINOv2 tokens joint dropout (for CFG)	0.1		
Attention mask when dropout (for CFG)	Semantic-to-pixel mask		
λ_d	0.1		
λ_{hyb}	10.0		
τ_{gate}	10.0		
τ_{rep}	0.2		
Sampling			
ODE solver	Heun [15]		
ODE steps	50		
Time steps	linear in [0.0, 1.0]		
CFG scale sweep range	[1.0, 4.0]		
CFG interval	[0.1, 1] (if used)		

Specifically, in Sec. 3.2, we start from a minimal co-denoising setup. At this stage, the only additional component is the DINOv2 [32] branch in the feature preprocessing stage, where DINOv2-Base features are normalized using the dataset-level statistics computed in RAE [50]. For conditioning dropout, we adopt the standard independent dropout strategy, with class-label dropout set to 0.1 and DINOv2 feature dropout set to 0.2, applied separately rather than jointly. No attention

Table 7. **Comparison of architectural designs for visual co-denoising.** We compare baseline backbones, single-stream fusion strategies, and dual-stream fusion variants with different allocations of feature-specific and shared/dual-stream blocks. All variants keep the pixel stream depth fixed at 12 JiT blocks for fair comparison. JiT-B/16[‡] and JiT-B/16[†] denote widened variants with hidden dimensions increased from 768 to 1024 and 1088, respectively, to match the parameter counts of the dual-stream models. Blue rows mark the stronger variants used in subsequent analysis. Following previous works [1, 26], we mainly use FID as reference. We highlight the default setting of the dual-stream model architecture in V-Co in light blue .

Model	Backbone	#Params	#Feature-Specific Blocks	#Shared/Dual-Stream Blocks	CFG=1.0		
					FID↓	IS↑	
Baselines							
(a)	JiT-B/16 [26]	JiT-B/16	133M	-	-	32.54	49.5
(b)	JiT-B/16 [26]	JiT-B/16 [†]	261M	-	-	22.67	69.9
(c)	LatentForcing [1]	JiT-B/16	156M	2	10	13.06	102.2
Single-Stream JiT Architecture							
(d)	DirectAddition	JiT-B/16	156M	2	10	15.15	103.4
(e)	DirectAddition	JiT-B/16	177M	4	8	12.90	112.7
(f)	DirectAddition	JiT-B/16	198M	6	6	11.77	116.2
(g)	DirectAddition	JiT-B/16	220M	8	4	14.20	104.1
(h)	DirectAddition	JiT-B/16	241M	10	2	14.43	99.4
(i)	ChannelConcat	JiT-B/16	157M	2	10	14.33	107.7
(j)	ChannelConcat	JiT-B/16	178M	4	8	11.93	117.3
(k)	ChannelConcat	JiT-B/16	200M	6	6	11.23	119.0
(l)	ChannelConcat	JiT-B/16	221M	8	4	13.73	104.6
(m)	ChannelConcat	JiT-B/16	242M	10	2	14.60	99.7
(n)	TokenConcat	JiT-B/16	156M	2	10	14.70	103.8
(o)	TokenConcat	JiT-B/16	177M	4	8	12.59	112.8
(p)	TokenConcat	JiT-B/16	198M	6	6	12.35	116.7
(q)	TokenConcat	JiT-B/16	220M	8	4	14.31	104.4
(r)	TokenConcat	JiT-B/16	241M	10	2	14.97	99.4
(s)	TokenConcat	JiT-B/16 [‡]	265M	6	6	9.74	129.4
(t)	TokenConcat	JiT-B/16 [‡]	274M	8	4	11.43	118.1
(u)	TokenConcat	JiT-B/16 [‡]	284M	10	2	12.90	109.4
Dual-Stream JiT Architecture							
(v)	TokenConcat	JiT-B/16	260M	6	6	11.78	115.4
(w)	TokenConcat	JiT-B/16	260M	4	8	11.40	118.3
(x)	TokenConcat	JiT-B/16	260M	2	10	10.24	124.5
(y)	TokenConcat	JiT-B/16	260M	0	12	8.86	132.8

mask is used in this section. The DINOv2 denoising loss coefficient (*i.e.*, λ_d) is set to 0.1 from this stage onward. Starting from Sec. 3.3, we further refine the conditioning design. As shown in Tables 2 and 8, jointly dropping class labels and DINOv2 features yields the best performance, and we therefore adopt a joint dropout probability of 0.1 from this section onward. Moreover, the semantic-to-pixel attention mask achieves the strongest results in Table 2, and is thus used as the default setting in the subsequent experiments. In Sec. 3.4, we further introduce the perceptual-drifting hybrid loss to improve feature alignment during co-denoising. The corresponding hyper-parameters, including λ_{hyb} , τ_{gate} , and τ_{rep} , are introduced from this section onward. Finally, in Sec. 3.5, we compare noise-schedule shifting and RMS scaling for feature calibration. Since RMS scaling performs best in our ablation, we adopt it as the default calibration strategy in the final model.

B. Additional Ablations

Extended ablation of single-stream fusion strategies. In Table 7, we present additional quantitative results that complement Table 1 in the main paper. Specifically, we study different allocations of feature-specific and shared blocks under three interaction strategies: direct addition, channel concatenation, and token concatenation. Overall, we observe that a balanced design, with 6 feature-specific blocks and 6 shared blocks out of 12 total blocks, generally yields the best performance. For

Table 8. **Comparison of different label/DINO dropout strategies under unguided (i.e., CFG=1.0) and guided (i.e., CFG=2.9) generation.** The best and second best numbers are **bolded** and underlined. We highlight the default setting of joint dropout of class labels and DINOv2 features in V-Co in light blue .

Label Dropout Ratio	DINO Dropout Ratio	CFG=1.0		CFG=2.9	
		FID↓	IS↑	FID↓	IS↑
Independent Dropout					
0.1	0.1	7.01	136.37	3.77	189.38
0.1	0.2	7.28	136.84	3.59	189.69
0.1	0.3	7.78	129.55	3.73	188.38
0.2	0.1	7.50	128.84	4.11	175.04
0.2	0.2	7.47	131.44	3.98	180.24
0.2	0.3	9.04	117.94	4.11	173.21
0.3	0.1	8.80	117.98	4.38	165.06
0.3	0.2	8.40	122.23	4.09	172.15
0.3	0.3	9.57	114.64	4.52	165.55
Joint Dropout					
0.1	0.1	<u>5.38</u>	161.4	3.55	214.39
0.2	0.2	5.62	158.51	<u>3.18</u>	219.60
0.3	0.3	5.17	<u>159.92</u>	3.17	<u>219.41</u>

Table 9. **Ablation of the similarity-based gating s_i in Eq. (15).** We conduct an ablation using a simplified version of s_i , where the gate is replaced with a scalar value s instead of being dependent on real and generated samples. We report both unguided and guided FID and IS scores while sweeping the scalar s . Row with the best guided FID score is highlighted in light blue .

s	Unguided (CFG=1.0)		Guided (Best CFG > 1.0)	
	FID↓	IS↑	FID↓	IS↑
Scalar gate s				
0	15.72	80.1	8.13	114.4
0.001	11.24	114.7	4.24	171.7
0.01	11.81	109.9	4.46	165.6
0.1	13.22	99.2	5.35	151.6
0.5	10.40	186.0	5.68	253.3
0.9	5.48	174.7	2.75	233.9
0.99	5.33	183.4	2.83	246.7
0.999	5.41	182.6	2.76	249.8
Similarity-Based Gating s_i (Default in V-Co)				
s_i	5.17	181.6	2.61	243.9

the token-concatenation strategy, we further examine widened variants by increasing the hidden dimension from 768 to 1024, resulting in models with 265M to 284M parameters. Nevertheless, none of these variants surpasses our default dual-stream co-denoising design, which achieves the best performance with 260M parameters.

Extended ablation of label and DINOv2 dropout strategies. In Table 8, we provide additional quantitative results complementing Table 2 in the main paper. Specifically, we evaluate different dropout ratios for labels and DINOv2 features, applied either independently or jointly. The results indicate that independently dropping labels or DINOv2 features generally underperforms joint dropout. As discussed in the main paper, once the unconditional prediction is structurally defined through semantic-to-pixel masking, removing all conditioning inputs from the pixel branch during training leads to better alignment with inference-time behavior.

Ablation of the similarity-based gating s_i in Eq. (15). To evaluate the effectiveness of the proposed similarity-based gating mechanism, we conduct an ablation where the adaptive gate s_i is replaced with a scalar value s , removing its dependence on real and generated samples. Under this simplification, the hybrid potential becomes $V_{\text{hyb}}(\mathbf{u}_i) = s \cdot V_{\text{pos}}(\mathbf{u}_i) - (1 -$

Table 10. **Comparison of different repulsion temperatures τ_{rep} .** We report both unguided and guided FID and IS scores by sweeping the repulsion temperature τ_{rep} . We highlight the rows with the best guided FID scores in light blue .

τ_{rep}	Unguided (CFG=1.0)		Guided (Best CFG> 1.0)	
	FID↓	IS↑	FID↓	IS↑
2e-3	4.97	186.4	2.72	251.3
2e-2	4.92	186.7	2.66	251.7
2e-1	5.17	181.6	2.61	243.9
2	5.33	180.1	2.64	244.8
2e1	5.30	180.7	2.67	247.7

Table 11. **Comparison of different gate temperatures τ_{gate} .** We report both unguided and guided FID and IS scores by sweeping the gate temperature τ_{gate} . We highlight the rows with the best guided FID scores in light blue .

τ_{gate}	Unguided (CFG=1.0)		Guided (Best CFG> 1.0)	
	FID↓	IS↑	FID↓	IS↑
1e-2	11.66	112.2	4.01	173.5
1e-1	10.96	114.6	4.06	173.6
1	7.34	136.9	3.10	189.6
1e1	5.41	108.8	2.75	247.7
1e2	5.17	181.6	2.61	243.9
1e3	5.11	185.8	2.77	252.2

Table 12. **Comparison of different hybrid loss coefficients λ_{hyb} .** We report both unguided and guided FID and IS scores by sweeping the hybrid loss coefficients λ_{hyb} . We highlight the rows with the best guided FID scores in light blue .

λ_{hyb}	Unguided (CFG=1.0)		Guided (Best CFG> 1.0)	
	FID↓	IS↑	FID↓	IS↑
1e-2	7.10	139.6	3.30	187.0
1e-1	6.72	142.5	3.17	189.9
1	5.23	162.5	2.74	214.0
1e1	5.17	181.6	2.61	243.9
1e2	13.61	133.4	4.49	221.4
1e3	31.30	79.3	17.90	124.4
1e4	65.84	41.8	58.04	56.0

$s) \cdot V_{\text{neg}}(\mathbf{u}_i)$. We report both unguided and guided FID and IS scores while sweeping the scalar s . As shown in Table 9, the default similarity-based gating in V-Co achieves the best guided FID score compared with the simplified scalar gate s , demonstrating the effectiveness of our design.

Hyper-parameter tuning for the perceptual-drifting hybrid loss. In Tables 10 to 12, we perform hyper-parameter sweeps over the three key hyper-parameters in the perceptual-drifting hybrid loss: the repulsion temperature τ_{rep} , the gate temperature τ_{gate} , and the hybrid loss coefficient λ_{hyb} . The default hyper-parameters used in V-Co are selected from these settings based on the best guided FID scores.

Comparison of different DINOv2 model sizes. In Table 13, we compare V-Co trained with DINOv2 features of different model sizes as semantic representations for co-denoising with pixels. For each DINOv2 model, we re-compute the feature scaling factor based on its RMS value to ensure that the SNR ratio between the DINOv2 features and pixels remains consistent. We also sweep over different DINOv2 diffusion loss coefficients λ_d , as different encoder sizes may perform best under different loss scales. The results show that even relatively small representation encoders preserve sufficient low-level detail for co-denoising. A similar trend has also been reported in Table 15(b) of RAE [50], Figure 3(b) of iREPA [35], and Table 2 of REPA [47]. REPA [47] attributes this behavior to the fact that all DINOv2 models are distilled from DINOv2-g and therefore share similar representations.

Table 13. **Comparison of different DINOv2 model sizes.** We report both unguided and guided FID and IS scores while sweeping the DINOv2 diffusion loss coefficient λ_d over $\{1e-3, 1e-2, 1e-1, 1\}$. We highlight the rows with the best guided FID scores in light blue for each DINOv2 model size.

Model	λ_d	#Params	Unguided (CFG=1.0)		Guided (Best CFG > 1.0)	
			FID↓	IS↑	FID↓	IS↑
DINOv2-Small	1e-3	22M	9.04	118.2	5.06	156.4
DINOv2-Small	1e-2	22M	6.70	134.4	3.67	176.2
DINOv2-Small	1e-1	22M	6.35	140.0	4.11	174.8
DINOv2-Small	1	22M	9.05	126.0	7.97	145.3
DINOv2-Base	1e-3	86M	12.27	107.7	6.45	151.9
DINOv2-Base	1e-2	86M	9.81	118.2	5.16	163.2
DINOv2-Base	1e-1	86M	8.83	120.6	5.54	154.8
DINOv2-Base	1	86M	16.77	95.1	16.48	106.9
DINOv2-Large	1e-3	304M	13.92	96.3	6.59	143.1
DINOv2-Large	1e-2	304M	9.19	119.9	4.20	173.8
DINOv2-Large	1e-1	304M	8.70	124.3	4.57	174.7
DINOv2-Large	1	304M	32.28	82.2	25.32	94.0
DINOv2-Giant	1e-3	1.1B	13.15	99.3	7.46	143.4
DINOv2-Giant	1e-2	1.1B	10.41	112.1	5.42	160.5
DINOv2-Giant	1e-1	1.1B	8.91	120.1	5.00	166.7
DINOv2-Giant	1	1.1B	23.02	83.4	24.18	95.9

C. Generated Samples

In Figs. 6 to 8, we present *uncurated* ImageNet 256×256 samples generated by V-Co-H/16 after 300 epochs of training, conditioned on the specified classes. Unlike the common practice of using a larger CFG value for visualization, we instead show samples generated with the same CFG value (1.5) used to obtain the reported FID of 1.71.

D. Limitation and Future Work

While V-Co provides a clear and effective recipe for visual co-denoising in pixel-space diffusion, several limitations remain. First, our study focuses on class-conditional generation on ImageNet-256, which offers a controlled setting for isolating the effects of architecture, CFG design, auxiliary objectives, and feature calibration, but does not capture the full diversity of generation settings such as open-ended text-to-image synthesis or more structured multimodal tasks. Extending the proposed recipe beyond ImageNet-style class conditioning is therefore an important direction for future work.

Second, V-Co relies on pretrained semantic features from a strong external visual encoder (*i.e.*, DINOv2). While this design is well aligned with our representation-alignment perspective and substantially improves semantic supervision in pixel-space generation, the resulting co-denoising dynamics may still depend on the quality, inductive biases, and spatial granularity of the teacher representation. Exploring alternative semantic feature sources is another promising direction.

Finally, our method is intentionally minimalist and does not incorporate stronger auxiliary supervision, such as combining REPA-style objectives with our perceptual-drifting hybrid loss. This keeps the empirical conclusions clean, but future works may explore how the V-Co recipe interacts with richer objectives and stronger supervision.



class 012: house finch, linnet, *Carpodacus mexicanus*



class 014: indigo bunting, indigo finch, indigo bird, *Passerina cyanea*



class 042: agama



class 081: ptarmigan



class 107: jellyfish



class 108: sea anemone, anemone



class 110: flatworm, platyhelminth



class 117: chambered nautilus, pearly nautilus, nautilus



class 130: flamingo



class 279: Arctic fox, white fox, *Alopex lagopus*

Figure 6. *Uncurated* samples on ImageNet 256×256 using V-Co-H/16 conditioned on the specified classes. Unlike the common practice of visualizing with a higher CFG, here we show images using the CFG value (1.5) that achieves the reported FID of 1.71.



class 288: leopard, Panthera pardus



class 309: bee



class 349: bighorn, bighorn sheep, cimarron, Rocky Mountain bighorn



class 397: puffer, pufferfish, blowfish, globefish



class 425: barn



class 448: birdhouse



class 453: bookcase



class 458: brass, memorial tablet, plaque



class 495: china cabinet, china closet



class 500: cliff dwelling

Figure 7. *Uncurated* samples on ImageNet 256×256 using V-Co-H/16 conditioned on the specified classes. Unlike the common practice of visualizing with a higher CFG, here we show images using the CFG value (1.5) that achieves the reported FID of 1.71.



class 658: mitten



class 661: Model T



class 718: pier



class 724: pirate, pirate ship



class 725: pitcher, ewer



class 757: recreational vehicle, RV, R.V.



class 779: school bus



class 780: schooner



class 829: streetcar, tram, tramcar, trolley, trolley car



class 853: thatch, thatched roof

Figure 8. *Uncurated* samples on ImageNet 256×256 using V-Co-H/16 conditioned on the specified classes. Unlike the common practice of visualizing with a higher CFG, here we show images using the CFG value (1.5) that achieves the reported FID of 1.71.